Corticocortical signaling drives activity in a downstream area rapidly and scalably

Xiaojian Li[1], Naoki Yamawaki[1], John M. Barrett[1], Konrad P. Körding[1,2], Gordon M. G. Shepherd[1*]

[1]Department of Physiology, Feinberg School of Medicine, Northwestern University, Chicago, Illinois, USA;

[2]Department of Physical Medicine and Rehabilitation, Feinberg School of Medicine, Northwestern University, Chicago, Illinois, USA;

*For correspondence: g-shepherd@northwestern.edu

How effectively does activity in an upstream cortical area drive activity in a downstream area? To address this, we combined optogenetic photostimulation with multi-unit electrophysiology to study a parietofrontal corticocortical pathway from retrosplenial cortex to posterior secondary motor cortex in mice. Photostimulation in the upstream area produced local activity that decayed quickly. This activity in turn drove downstream activity that arrived rapidly (5-10 ms latencies), and scaled in amplitude across a wide range of stimulus parameters as an approximately constant fraction (~0.2) of the upstream activity. A model-based analysis could explain the corticocortically driven activity with exponentially decaying kernels (~20 ms time constant) and small delay. Reverse (antidromic) driving was similarly robust. The results show that corticocortical signaling in this pathway drives downstream activity in a mostly linear manner. The regular and

predictable responses further suggest that precise stimulation driven control of cortical population activity should be possible.

INTRODUCTION

Corticocortical pathways support inter-areal communication, which is central to behavior (Felleman and Van Essen, 1991; Misic and Sporns, 2016). Connectomics studies in both humans and animal models have identified a structural basis for many corticocortical pathways (Oh et al., 2014; Zingg et al., 2014; Jbabdi et al., 2015; Glasser et al., 2016; Bassett and Sporns, 2017), and optogenetic mapping studies in rodents have begun to characterize dynamic signaling at the mesoscopic scale (Lim et al., 2012). However, the functional properties of inter-areal signaling in these pathways have been challenging to resolve, particularly for higher-order pathways that are many synapses removed from the sensory periphery and thus difficult to activate in a spatiotemporally precise manner with natural stimuli. Extracellular electrical stimulation has been used in efforts to artificially generate focal activity, but is inherently limited due to its nonspecificity, antidromic activation, and other issues (Nowak and Bullier, 1998; Histed et al., 2009). More work is needed to understand the dynamics of corticocortical signaling.

Recently developed optogenetic methods promise a more precise approach towards characterizing corticocortical communication. They have enabled detailed characterization of cell-type-specific connections in long-range circuits *ex vivo* (Petreanu et al., 2007; Petreanu et al., 2009). They have enabled the characterization of inter-areal corticocortical circuits in mice at the cellular level (Mao et al., 2011; Hooks et al., 2013; Yang et al., 2013; Kinnischtzke et al., 2014; Petrof et al., 2015; Suter and Shepherd, 2015; Kinnischtzke et al., 2016; Sreenivasan et al., 2016). They have also been used *in vivo* to characterize how optogenetically evoked activity

interacts with sensory input at the level of the cortex (e.g. (Manita et al., 2015)). However, they have not yet been exploited to characterize in detail how optogenetically evoked activity propagates between cortical areas, particularly for higher-order areas that are deep within the corticocortical network and therefore inaccessible for discrete activation by sensory stimuli.

A newly characterized higher-order corticocortical pathway goes from retrosplenial cortex (RSC) to posterior secondary motor cortex (M2) (Yamawaki et al., 2016). RSC axons innervate M2 neurons broadly across all layers and projection classes, forming a synaptic circuit whereby RSC, which receives input from dorsal hippocampal networks and is involved in spatial memory and navigation, appears to communicate with M2, which sends output to diverse motor-related areas and appears to be involved in diverse sensorimotor functions. As such, this connection is an interesting target for the reverse engineering of corticocortical connections.

What kind of dynamic signaling is supported by the cellular connections in this RSC→M2 pathway? We may expect interactions to be nonlinear; every neuron is nonlinear through its spiking mechanism, there are many types of connections, and the neurons are organized into a nonlinear recurrent system. Alternatively, we may expect that the system actively linearizes itself (Bernander et al., 1994). Characterizing corticocortical interactions is important as it promises to inform many theories of neural computation (Arbib, 2002; Ermentrout and Terman, 2010).

How strongly might signaling along the RSC→M2 pathway be driven when probed with photostimulation? It might be very strong; after all, photostimulation may incite many more neurons to spike than typical stimuli. Alternatively, we may expect it to be weak; after all, M2 receives only a fraction of its inputs from RSC. Indeed, corticocortical signaling may only

69 modulate activity driven by other inputs and have very little impact on its own (Sherman and
70 Guillery, 2011). These questions again speak to ways of theorizing about neural computation.

71 Here we sought to answer these questions by developing an approach for assessing and
72 manipulating corticocortical circuit dynamics in the intact brain. We used stereotaxic viral
73 injections to express ChR2 in presynaptic RSC neurons (Yamawaki et al., 2016), and developed
74 *in vivo* methods in the anesthetized mouse for sampling photo-evoked multi-unit activity in M2
75 driven by RSC photostimulation. Duplication of the setup to permit both stimulation and
76 recording at both ends of the RSC→M2 projection allowed a detailed parametric characterization
77 of both local (upstream) and downstream activity evoked both ortho- and antidromically. This
78 allowed us to carefully measure the influence inter-areal signaling as a function of stimulation
79 amplitude, duration, and the area being stimulated.

80

81 **RESULTS**

82 To investigate corticocortical signaling in the RSC→M2 pathway, we used viral methods to label
83 neurons with ChR2, optical fibers to photostimulate them, and linear arrays to record the evoked
84 activity. Similar to previous studies of this pathway (Yamawaki et al., 2016), we infected
85 neurons in RSC with an AAV encoding ChR2 and a fluorescent protein (**Fig. 1A,B**). After a
86 recovery period of several weeks, animals were anesthetized with ketamine and underwent
87 placement of photostimulation fibers and silicon probes in the RSC and M2 (**Fig. 1C**).

88

89 **RSC photostimulation drives downstream M2 activity**

90 To understand how RSC affects M2 activity, we photostimulated in RSC and measured multi-
91 unit activity in M2 (**Fig. 2A**). In single trials, activity was typically detected on multiple channels

(**Fig. 2B**). Over repeated trials, on channels showing responses, photostimulation reliably evoked spiking activity (**Fig. 2C**). The peristimulus time histogram shows clear stimulus triggered activity (**Fig. 2D, top**). These histograms of M2 activity showed robust, transient increases in activity starting with a short delay after the onset of photostimulation in RSC.

It is important to understand how the virus and the construct might affect the responses. We therefore performed parallel experiments with two different AAV serotypes carrying different variants of ChR2 driven by different promoters: AAV1-ChR2-Venus, carrying wild-type ChR2 driven by the CAG promoter, and AAV9-ChR2-eYFP, carrying ChR2 with the H134R mutation driven by the CaMKII promoter (see Methods). The two viruses gave similar responses (**Fig. 2D**), an impression that was borne out in further detailed comparisons that will be presented in later sections. Our findings suggest that our strategy is not overly affected by details of the virus or construct.

We need to be sure that the M2 responses reflect synaptically driven spikes of postsynaptic M2 neurons, rather than spikes in presynaptic axons. We therefore sampled M2 responses before and after injecting M2 with muscimol, a GABA agonist, which suppresses spiking in cortical neurons while preserving presynaptic spiking (Chapman et al., 1991; Chatterjee and Callaway, 2003). As expected, muscimol injection abolished most of the activity in M2 (3 of 3 animals) (**Fig. 2E, top**), whereas injection of saline had no effect (2 of 2 animals). Thus, M2 responses are, indeed, driven by corticocortical synaptic activity.

We also want to be sure that our results cannot be overly affected by probe placement. In earlier pilot experiments the probe was sometimes inadvertently placed slightly lateral by ~0.5-1 mm, resulting in recordings in M1 instead of M2. In this case we observed little or no photo-evoked activity (**Fig. 2E, bottom**), consistent with the anatomy and electroanatomy of the

RSC→M2 projection, which provides little or no direct input to M1 neurons (Yamawaki et al., 2016). Mistaken probe placement would thus simply decrease the observed activity.

From the results of these initial characterizations we conclude that (i) optogenetically stimulating RSC drives a delayed, brief wave of spiking activity in M2; (ii) the evoked activity appears to reflect mostly the properties of the corticocortical circuit itself rather than the those of the viruses and/or constructs; and (iii) the M2 activity appears to arise from orthodromically driven signaling along the RSC→M2 corticocortical pathway, rather than non-specific (e.g. cortex-wide) activation. Next, we turned to a more in-depth characterization of the technique by recording in both areas.

Comparison of local RSC and downstream M2 activity evoked by RSC photostimulation

To better understand signaling in the RSC→M2 circuit, we recorded from both the RSC and M2 during RSC photostimulation, allowing us to assess both the locally driven activity in upstream RSC and the orthodromically driven activity in downstream M2 (**Fig. 3A**). As observed with both AAV9-ChR2 (**Fig. 3B-F**) and AAV1-ChR2 (**Fig. 3G-K**), with RSC photostimulation the activity recorded in RSC rose rapidly at the onset of photostimulation and declined rapidly as well, whereas activity recorded in M2 followed with a brief latency (in ms after the RSC peak: 7.5 for AAV9, and 6.5 for AAV1) and rose to lower levels than observed in RSC (RSC/M2 amplitude ratio: 3.8 for AAV9, 4.1 for AAV1). The results of this two-probe characterization of RSC photostimulation thus reveal two important aspects of corticocortical driving. First, at the upstream end there is a rapid and strong decay of the local activity in the directly photostimulated RSC (**Fig. 3B,G**). This decay is generally consistent with ChR2 desensitization (Lin et al., 2009), and the greater decay observed with AAV1 is consistent with the reduced

desensitization of ChR2-H134R mutation (in AAV9) compared to wild-type ChR2 (in AAV1) (Nagel et al., 2003; Nagel et al., 2005). Second, at the downstream end the corticocortically driven activity in M2 was reduced in amplitude and slightly delayed relative to the RSC activity. A caveat is that these properties might not be generalizable, reflecting instead the particular photostimulus parameters used in these experiments. Therefore, we next investigated in detail the stimulus dependence of the responses by exploring a wide range of stimulus intensities and durations.

Parametric characterization of orthodromic (forward) driving

Key parameters for the dynamics of a circuit are the dependency on stimulus amplitude (light intensity) and duration (pulse width). Stimulus trials were delivered at five different intensities (20, 40, 60, 80, and 100% relative to maximum) and durations (1, 5, 10, 20, and 50 ms), with random interleaving and many repetitions (typically 30 trials per experiment) for each of the 25 unique intensity-duration combinations (**Fig. 4A**). Responses on the local RSC probe and the downstream M2 probe were averaged across trials as before, and the median responses were determined across animals (AAV9 data shown in **Fig. 4B,C**; AAV1 data shown in **Fig. 4–figure supplement 1**). Clearly, the evoked activity in both RSC and M2 varied with stimulus parameters. To assess how response properties might depend systematically on stimulus parameters, we developed a simple model, and performed several further analyses.

A simple two-stage model captures the major features of orthodromic driving

To better understand the responses we want to fit a simple model to the data. Visual inspection of the waveforms of both the RSC and M2 responses (**Fig. 4**) shows roughly linear increases with

intensity. Clearly, activity in the photostimulated RSC decays rapidly and extensively, consistent with ChR2 densensitization (as discussed above). However, in the downstream M2, it is unclear how responses scale directly with upstream RSC activity; for example, do they scale linearly, or show signs of adaptation? We would like a simple model to allow us to both describe and interpret the data.

Explorative data analysis revealed that we could fit the directly stimulated (upstream) area well with briefly delayed activation followed by a large and rapid decay (**Fig. 5A**). Hence, we modeled stimulation as a time-shifted delta function divided by a linear function of the integral of the stimulus history. So this first-stage model has 3 parameters for gain, delay, and the steady state adaptation. These parameters seem intuitively necessary: the gain describes basic physiology; the delay is needed due to the ~3 ms blanking of the stimulus artifact (see Methods), but can also account for ChR2 activation kinetics; adaptation is expected from ChR2 inactivation/desensitization kinetics, and allows for additional factors contributing to a temporal decline in activity (e.g. GABA release, synaptic depression).

Indeed, we found this model to produce good fits when we analyzed activity in the stimulated (RSC) area. We find that the model qualitatively describes the data, describing both its initial rise, and its decay over time (AAV9 data shown in **Fig. 5B,C**; AAV1 data shown in **Fig. 5–figure supplement 1A,B**). In fact, it has high R^2 values on both the AAV9 (0.93) and the AAV1 (0.83) datasets. This suggests that the bulk of the stimulation effect is described by an essentially immediate stimulus followed by considerable decay.

Explorative data analysis revealed that we could fit the indirectly stimulated (downstream) area well with thresholded activation without decay, or adaptation (**Fig. 5A**) in terms of the activity of the stimulated area. We modeled this as an exponentially decaying kernel

with temporal integration and a threshold. So this second-stage model has 4 parameters for gain, threshold, kernel time-constant, and baseline. These 4 parameters again seem intuitively necessary: the gain describes basic physiology; sufficiently weak stimulation produces little activity; there is a slow transmission of information; and, there is non-zero baseline activity in the downstream area. Adding an explicit delay parameter to the model was not necessary: the combination of thresholding and slow stimulus integration sufficed to reproduce the experimentally observed the delay.

We found this model to produce good fits in the downstream (M2) area. We find that the model qualitatively describes the data, describing both its slow rise, and its subsequent decay over time (AAV9 data shown in **Fig. 5D,E**; AAV1 data shown in **Fig. 5–figure supplement 1C,D**). It also describes how in some conditions there is no activation whatsoever. This model also has high R^2 values on both the AAV9 (0.70) and the AAV1 (0.65) datasets. The time constants of the fitted exponential kernels were on the order of a few tens of milliseconds (20 ms for AAV9 and 32 ms for AAV1 data), which combines many aspects, including synaptic current, membrane constants, and is also comparable to the time constants of fast spike adaptation in cortical excitatory neurons (La Camera et al., 2006; Wark et al., 2007; Suter et al., 2013). This suggests that the bulk of the stimulation effect is described by an arrival of stimulation which decays exponentially over time.

Analysis of orthodromically driven responses

Next, we assessed whether the reduced amplitude of M2 responses (compared to upstream RSC activity, discussed above) was a consistent property across stimulus parameters. Plotting the response amplitudes in RSC and M2 for all 25 stimulus combinations (**Fig. 6A**) showed that

these ranged widely but with a consistent relationship, substantially greater in RSC than in M2. The same pattern was observed for both viruses (factor of 4.7 for AAV9 and 6.8 for AAV1 experiments), even though absolute response amplitudes were generally stronger for AAV9 compared to AAV1 (1.5-fold for RSC responses and 2.1-fold for M2 responses; $p < 10^{-3}$, sign test). Overall, the 'driving ratio', the ratio of the remotely driven activity in M2 relative to the locally driven activity in RSC, was ~0.2 (**Fig. 6B**). In other words, activity in the downstream area, M2, was generally about a fifth of that in RSC, across a wide range of stimulus parameters.

Of further importance to the interaction are latencies. These also showed a consistent relationship, with M2 responses peaking with a short delay after RSC responses (**Fig. 6C**). The same pattern was observed for both viruses (median latency of M2 response relative to RSC response of 8 ms for AAV9 and 7 ms for AAV1 experiments). In this case, unlike the absolute response amplitudes, the latencies of the responses in RSC and M2 did not differ significantly for AAV9 vs AAV1 ($p > 0.05$, sign test). In contrast to the amplitudes, the latencies were largely stimulus-independent.

Response amplitudes in both areas clearly varied systematically and substantially for different combinations of stimulus intensity and duration (**Fig. 4B,C; Fig. 6A**), but how? Plotting the RSC responses as a function of stimulus intensity showed a linear dependence (**Fig. 6–figure supplement 1A,B**). In contrast, plotting the same RSC responses as a function of stimulus duration showed a sub-linear dependence (**Fig. 6–figure supplement 1C,D**). Applying the same analysis to the modeled traces gave qualitatively similar results (**Fig. 6–figure supplement 1**, bottom row of plots).

The M2 responses showed a similar, albeit noisier, set of patterns, with roughly linear intensity-dependence (**Fig. 6–figure supplement 2A,B**) and sub-linear duration-dependence

(**Fig. 6–figure supplement 2C,D**). Applying the same analysis to the modeled traces again gave qualitatively similar results (**Fig. 6–figure supplement 2**, bottom row of plots). Results with AAV1-ChR2 showed similar patterns (data not shown).

Driving in reverse: antidromic propagation

The photoexcitability of ChR2-expressing axons (Petreanu et al., 2007) has previously been exploited in *in vivo* experiments to antidromically drive a trans-callosal corticocortical projection (Sato et al., 2014). Here, our experimental set-up (**Fig. 2**) allowed us to similarly drive the RSC→M2 projection in reverse, as a way to gain additional insight into signaling properties in this system. Characterization of antidromic optogenetic driving is additionally of technical interest both as an intended (e.g. (Sato et al., 2014)) or unintended effect of focal photostimulation in an area containing ChR2-expressing axons. Using the same labeling strategy (i.e., AAV-ChR2 in RSC) and recording (i.e., electrodes in both RSC and M2) arrangement, in the same experiments we also delivered photostimuli to M2 (via a second optical fiber) as a way to activate ChR2-expressing axons there (i.e., projecting from RSC) and thereby gain insight into the properties of antidromic signaling in the same RSC→M2 pathways (**Fig. 7A**).

In particular, we wondered if antidromic activation would result in similar or different effects compared to orthodromic activation. Photostimulation in M2 resulted in a short-latency, short-duration wave of antidromically generated activity in both RSC and a similar but smaller-amplitude wave of locally generated activity in M2. Similar results were found for experiments with AAV9 (**Fig. 7B-F**) and AAV1 (**Fig. 7G-K**). Neither amplitudes nor latencies differed with antidromic activation for the 10-ms, 100% stimulus combination. However, across all stimulus combinations the response amplitudes were overall ~2-fold greater in RSC relative to M2 (**Fig.**

7L), contrasting with the reduced amplitude in the downstream area observed with orthodromic stimulation. Similar to orthodromic stimulation, absolute response amplitudes were generally stronger for AAV9 compared to AAV1 (2.6-fold for RSC responses and 3.8-fold for M2 responses; $p < 10^{-3}$, sign test). Latencies in the two areas were indistinguishable with AAV1 and slightly delayed (by 3 ms) in M2 with AAV9 (**Fig. 7M**). Latencies in RSC were slightly shorter with AAV9 than AAV1 (by 2.5 ms; $p < 10^{-4}$, sign test), but those in M2 were the same with the two viruses ($p > 0.05$, sign test). These results indicate that RSC axons forming this corticocortical projection can be robustly activated in M2, generating activity both locally in M2 and antidromically in RSC – which is in effect the 'downstream' area in this experimental configuration.

Laminar analysis

Lastly, we considered the laminar profile of M2 activity generated by activation of the RSC→M2 pathway. As in the previous experiments involving orthodromic activation, we injected virus into the RSC, and subsequently inserted the silicon probe (32 channels and 50 µm spacing) to record downstream activity in M2. The probe was inserted leaving several contacts out of the cortex; the depth of penetration was estimated both by viewing the site of entry with a high-power stereoscope, and by assessing channel noise variance, which was low for contacts outside cortex (see Methods) (**Fig. 8A,B**). Group analysis ($n = 9$ mice injected with AAV1-ChR2) of activity across channels indicated a bias towards deeper layers (**Fig. 8C,D**). Previous slice-based characterization of RSC→M2 connectivity indicated that RSC axons form monosynaptic excitatory synapses onto postsynaptic M2 neurons across all layers and major classes of projection neurons, including upper-layer neurons (Yamawaki et al., 2016). Because

276 those experiments were performed in whole-cell voltage-clamp mode, here, to explore the
277 cellular basis for the preferential activation of deeper layers in M2 we performed similar brain
278 slice experiments but with cell-attached current-clamp recordings, allowing assessment of the
279 efficacy of RSC inputs in generating suprathreshold (spiking) activity in M2 neurons.
280 Comparison of layer 2/3 and layer 5 neurons showed significantly greater tendency of photo-
281 activated RSC axons to generate spikes in layer 5 neurons (**Fig. 8E**), consistent with the laminar
282 profile recorded *in vivo* (**Fig. 8C,D**). The laminar distribution of activities thus indicates that
283 RSC drives M2 neurons across multiple layers, particularly the middle and deeper layers.
284 Because these layers contain projection neurons with diverse outputs to the pons, midbrain,
285 thalamus, and more, this result reinforces the idea that RSC→M2 corticocortical signaling can
286 serve as a robust conduit for information along this parietofrontal pathway.
287
288 **DISCUSSION**
289 We analyzed corticocortical signaling in the RSC→M2 pathway *in vivo* using optogenetic
290 photostimulation and electrophysiology. Across a wide range of stimulus parameters, the
291 downstream responses arrived rapidly and scaled systematically with the photo-evoked activity
292 in the upstream area. We found that a simple model involving linear integration, delay, and
293 thresholding could describe much of the data.
294 In using optogenetic photostimulation to analyze this circuit we did not attempt to mimic
295 naturalistic activity patterns of the RSC but rather used this as a tool to perturb the circuit
296 (Miesenbock, 2009). This approach allowed us to systematically vary the stimulus intensity and
297 duration and assess whether and how response properties depended on input parameters. Another
298 artificial aspect of these experiments was the use of anesthesia, without which extensive

parametric testing would have been challenging with head-fixed animals. Our approach is aimed at understanding computational aspects of corticocortical population signaling, rather than how detailed corticocortical signals relate to the high-dimensional aspects of behavior (Carandini, 2012).

We found that a simple two-stage model captured the broad features of the data. At the upstream end, the conversion of light energy into local spiking activity in the upstream area (the RSC) could be described as a simple transfer function dominated by strong and rapid decay. The decay likely reflects primarily ChR2 desensitization, a property common to all ChR2 variants including the two used here (Nagel et al., 2003; Nagel et al., 2005; Lin et al., 2009). Additional components of the decay may have come from endogenous factors associated with the neurons and microcircuits in the locally stimulated area (e.g. GABA release from inhibitory interneurons, short-term synaptic depression). One potential application of this first-stage model of the local photoactivation process is that it could be used to design photostimuli that precisely compensate for the decay.

At the downstream end, the conversion of upstream activity (in RSC) into downstream activity (in M2) could be described by a simple exponential process with a brief delay, and no adaptation mechanism. Although a small non-linearity was included in the form of a threshold, the efficacy of the model suggests that corticocortical signaling is mostly linear. The efficacy of the second-stage model implies that corticocortical driving of downstream activity is highly scalable. It also implies that adaptation is not a major factor in shaping the downstream response, at least on the short time scales (tens of milliseconds) studied here. However, some contribution of an adaptation process may be reflected in the early component of the responses, which tend to be larger than the fitted traces. Whether this simple model can describe corticocortical signaling

in other inter-areal pathways remains to be determined, but similarities between our findings using optogenetic activation and related work in the visual system (e.g. (Carandini et al., 1997)) suggest this is plausible.

The scalability of corticocortical signaling observed here may be particular to the RSC→M2 pathway, or may represent a more general computational principle of cortical operation (Miller, 2016; Rolls, 2016). Although cortical circuit organization appears basically conserved, areas can also differ substantially in their quantitative properties (Harris and Shepherd, 2015). Corticocortical signaling in other pathways might therefore be expected to exhibit broadly similar scalability, but with pathway-specific differences in the details of spatiotemporal dynamics. The ability to capture both general and pathway-specific features of corticocortical signaling in a simple mathematical model suggest a utility of this approach both for theoretical approaches to cortical network modeling (Bassett and Sporns, 2017) and for neural engineering approaches in which closed-loop neural dynamics and behavioral control require predictive modeling (Grosenick et al., 2015). Further studies will be needed to test these speculations.

The downstream response latencies (~8 ms after upstream responses), together with the RSC-M2 inter-areal distance of ~2 mm and allowing for the timing of synaptic transmission (Sabatini and Regehr, 1999), implies a conduction speed for these RSC→M2 corticocortical axons on the order of 0.3 m/s, a typical value for thin unmyelinated cortical axons (Raastad and Shepherd, 2003). The consistency of the latency across different stimulus parameters suggests that the RSC→M2 circuit was activated in a similar manner independent of the particular activity level of the RSC neurons; in particular, this suggests that the M2 activity resulted from direct excitatory RSC input to M2 neurons, rather than polysynaptic pathways via posterior parietal

345 cortex or anterior thalamus (Yamawaki et al., 2016) or hippocampus (Sugar et al., 2011). Had
346 polysynaptic interactions been increasingly engaged by longer-duration stimuli, responses should
347 have increased over time in both RSC and M2, not decreased as observed.

348 In addition to robust forward (orthodromic) activation, we found robust reverse
349 (antidromic) corticocortical signaling in RSC→M2 circuits. Antidromic driving, evoked by
350 stimulating in M2 the ChR2-labeled axons projecting from RSC, was notable for two distinct
351 properties. First, photostimulation in M2 (or ChR2-expressing axons of RSC neurons) generated
352 even more activity downstream in RSC than locally in M2, by a factor of ~2. Thus, the gain in
353 this corticocortical circuit (ratio of downstream to upstream activity) appeared to be a property
354 associated with the anatomical directionality of the projection (RSC→M2), rather than
355 determined by the site of stimulation. The greater activity in RSC could reflect locally abundant
356 axonal branches of the labeled RSC neurons. Second, the efficiency of information transmission
357 appeared similar in either direction; i.e., a property associated with the site of stimulation rather
358 than the anatomical directionality of the projection. Optogenetic antidromic activation has been
359 previously exploited used as a way to selectively generate activity in an area (e.g. (Sato et al.,
360 2014)). Our results thus not only provide an additional example of how a corticocortical pathway
361 can be driven in reverse to remotely generate activity in an area of interest, but identify key
362 similarities as well as differences compared to orthodromic driving.

363 Corticocortical signaling in the RSC→M2 pathway may be critical for conveying
364 information from hippocampus-associated networks involved in spatial memory and navigation
365 to cortical and subcortical networks involved in decision making and action planning and
366 execution (Vann et al., 2009; Sugar et al., 2011; Yamawaki et al., 2016). Consistent with this,
367 lesions of the RSC impair navigation without impairing either motor function or the ability to

recognize navigational landmarks (Maguire, 2001), and RSC pathology can be an early and prominent feature of Alzheimer's disease (Minoshima et al., 1997). Conversely, the RSC→M2 connectivity appears strengthened after damage to adjacent cortex in a mouse stroke model (Brown et al., 2009). Thus another potential application of experimental-theoretical paradigm developed here is to understand primary pathology and adaptive plasticity in corticocortical signaling in mouse models of disease.

MATERIALS AND METHODS

Animals. Studies were approved by the Northwestern University Animal Care and Use Committee, and followed the animal welfare guidelines of the Society for Neuroscience and National Institutes of Health. Wild-type mice (C57BL/6, female and male; Jackson Laboratory, Bar Harbor, ME) were bred in-house. Mice were 6-9 weeks old at the time of *in vivo* experiments.

Stereotaxic injections. Mice under deep anesthesia underwent stereotaxic injection of adeno-associated virus (AAV) carrying ChR2 into the RSC, following standard methods as previously described (Yamawaki and Shepherd, 2015; Yamawaki et al., 2016). Two viruses were used: AAV1.CAG.ChR2-Venus.WPRE.SV40 (AV-1-20071P, University of Pennsylvania Vector Core, Philadelphia, PA; Addgene #20071, Addgene, Cambridge, MA), and AAV9.CamKIIa.hChR2(H134R)-eYFP.WPRE.hGH (AV-9-26969P, Penn Vector Core; Addgene #26969P). Stereotaxic coordinates for the RSC were: −1.4 mm caudal to bregma, ~0.5

391 mm lateral to midline. To minimize cortical damage, the glass injection pipette was pulled to a
392 fine tip, beveled to a sharp edge (Micro Grinder EG-400, Narishige, Tokyo, Japan), and
393 advanced slowly into the cortex; injections were made slowly (over 3 minutes) at two depths (0.8
394 and 1.2 mm from pia, ~20 nL per injection). Mice were returned their home cages and
395 subsequently maintained for at least 3 weeks prior to experiments, to allow time for ChR2
396 expression levels to rise in the infected neurons.
397
398 Cranial hardware. Mice under deep anesthesia underwent placement of cranial mounting
399 hardware. A small skin incision was made over the cerebellum to expose the skull, and a
400 stainless-steel set screw (single-ended #8-32, SS8S050, Thorlabs, Newton, NJ), crimped with a
401 spade terminal (non-insulated, 69145K438, McMaster-Carr, Elmhurst, IL) was affixed with
402 dental cement to the skull. This set screw was later screwed into the tapped hole located at the
403 top of a 1/2" optical post used for head fixation.
404
405 *In vivo* circuit analysis: general procedures. Mice were anesthetized with ketamine-xylazine
406 (ketamine 80-100 mg/kg and xylazine 5-15 mg/kg, injected intraperitoneally), placed in the
407 recording apparatus, and head-fixed using the set screw as described above. Body temperature
408 was monitored with a rectal probe and maintained at ~37.0 °C via feedback-controlled heating
409 pad (FHC, Bowdoin, ME). Craniotomies were opened over the RSC and M2 using a dental drill,
410 just large enough (~1 mm) to allow passage of the linear arrays and the tips of the optical fibers.
411 During the subsequent recordings, ACSF was frequently applied to the exposed brain area to
412 prevent damage from dehydration. The level of anesthesia was continuously monitored based on

413 paw pinching, whisker movement, and eye-blinking reflex. Additional doses of anesthesia were
414 given (50% of induction dose) when required.
415
416 Photostimulation apparatus. An optical fiber (FG400AEA, multimode fiber, 0.22 NA, 400 µm
417 core, outer diameter 550 µm with coating; Thorlabs), mounted on a motorized micromanipulator
418 (Sutter Instrument, Novato, CA), was positioned directly over the region of the infected neurons
419 in the RSC (**Fig. 2A**). The tip of the fiber was ~0.5 mm away from the surface of the brain,
420 immersed in ACSF. In most experiments, a second fiber was similarly positioned directly over
421 the M2 (**Fig. 2A**). For each fiber, the light source was an LED (M470L3; Thorlabs), coupled to
422 the fiber by an adapter (SM1SMA; Thorlabs). The power was controlled using a commercial
423 (LEDD1B; Thorlabs) or LED driver (based on RCD-24-1.00 module; RECOM Lighting, Neu-
424 Isenburg, Germany). The output power of the LED driver was modulated by signal waveforms
425 delivered via a commercial multifunction (analog and digital) interface board (NI USB 6229;
426 National Instruments, Austin, TX) or by a signal generator based on a 32-bit microcontroller
427 board (Arduino Due with ARM Cortex-M3, Adafruit, New York, NY). The boards were also
428 used to send a short pulse train to digitally encode the start and other parameters of the light
429 waveform, sampled on the digital input port of the electrophysiology data acquisition (DAQ)
430 board (see **Fig. 2B**). Software tools (LabVIEW) included a GUI (GenWave) for generating and
431 transferring the waveforms to the LED controller. The LED driver was either internally software-
432 triggered (GenWave) or externally hardware-triggered by a digital signal. The system was
433 calibrated using a power meter to determine the relationship between input voltage to the driver
434 and the output intensity of the fiber, to determine the voltages (in the range of 0–5 V)
435 corresponding to 0, 20, 40, 60, 80, and 100% of the full power (6.1 mW, measured at the tip of

436 the optical fiber). During the experiment, analog voltages corresponding to these intensities were
437 sent to the LED driver.
438
439 Electrophysiology apparatus. The linear arrays used were 32-channel silicon probes with ~1 MΩ
440 impedance and 50-µm spacing (model A1×32-6mm-50-177, NeuroNexus, Ann Arbor, MI), in
441 either "triangular" or "edge" configuration. The probes were mounted on a motorized 4-axis
442 micromanipulator (Thorlabs MTSA1 linear translator mounted on a Sutter MP285 3-axis
443 manipulator), and positioned under stereoscopic visualization over the M2 at cortical surface
444 (i.e., entry point) coordinates of +0.6 mm rostral to bregma and 0.2 mm lateral to midline. The
445 probes were tilted by ~30° off the vertical axis for alignment with the radial axis of the cortex.
446 The probe was then slowly inserted into the cortex at a rate of 2 µm/s (controlled by software),
447 until it reached a depth of 1600 µm from the pia. In most experiments, a second array was
448 similarly inserted into the RSC (same stereotaxic coordinates as given above for the viral
449 injections), except that in this case the array was inserted perpendicular to the horizontal plane,
450 and the fiber was slightly tilted (**Fig. 2A**).
451 Signals were amplified using a RHD2132 amplifier board based on a RHD2132 digital
452 electrophysiology interface chip (Intan Technologies, Los Angeles, CA). The RHD2132 chip is
453 an AFE (analog front end) which integrates the analog instrument amplifiers, filters, analog-to-
454 digital converters, and microcontrollers in one chip. The SPI (serial peripheral interface) port is
455 used to configure the chip and to stream the bio-signal data to the DAQ board. The gain of the
456 amplifier was fixed at 96 × 2 = 192 (2-stage amplifier). The filter was set to an analog bandpass
457 of 0.1~ 7.5K Hz with a digital filter cutoff of 1Hz. Because the 32 channels of the bio-signal

458 inputs share the same 16 bit ADC with a multiplexer, and the maximum sample rate of the ADC
459 is 1.05M SPS, the single channel sample rate was set to 30K SPS.

460 For hardware control, we used a RHD2000 USB Interface Evaluation Board (Intan) or
461 DAQ board based on a breakout board with a XEM6010 USB/FPGA module (Opal Kelly,
462 Portland, OR), a field-programmable gate array (FPGA) with many digital I/O channels for
463 communicating with other digital devices and streaming in all the bio-signal data from the
464 RHD2000 amplifiers. The USB port of the module was linked with a USB cable to pipe the data
465 stream in or out the PC. The RHD2000 amplifier boards were connected to a DAQ board using
466 SPI interface cables in low-voltage differential signal mode, which is well suited for
467 communication via longer cables. In this experiment, the digital ports included in the DAQ board
468 were only used for acquiring the LED photostimulation parameters from the LED controller (see
469 **Fig. 2B**).

470 For data logging, The C++/Qt based experimental interface evaluation software (Intan)
471 was used for early stage evaluation. Then the original APIs (Rhythm USB/FPGA interface) were
472 all rebuilt and wrapped up into a LabVIEW-based SDK. All the software, including the amplifier
473 configuration, online visualization, data logging, and more, were developed from this SDK in
474 LabVIEW environment.

475

476 Trace analysis. Data were stored as the raw signal from the amplifiers, filtered by 60 Hz notch
477 filter. A strong photovoltaic effect contaminated the recordings on the photostimulated probe. To
478 reduce this, we used the following approach using LabVIEW (National Instruments) routines.
479 First, we used a digital high-pass filter (800 Hz cut-off, 2^{nd}-order Butterworth), which shrank the
480 photovoltaic artifact to the first 3 ms post-stimulus window. Then, a threshold detector

(Threshold Detector VI) was applied, with threshold set to 4 s.d. over a minimum of 3 continuous samples to detect spike peaks. Last, the spike count of the first 3 ms window was replaced by the average value of the pre-stimulus window of 20 ms. To generate peristimulus time histograms, we used the following approach using Matlab (Mathworks, Natick, MA) routines. Time stamps were determined for each detected spike. The time stamps of all the spikes of every channel were used to generate the peristimulus time histogram and raster maps. Responses were averaged across all channels in each trial, and then across multiple trials (typically ~40) to yield a mean histogram.

Laminar analysis. We estimated the depth of probe insertion in the cortex (and thus the cortical depth of each contact) based on the total displacement of the motorized manipulator holding the probe. In addition, because this estimate can be affected by the viscoelastic properties of brain tissue, we also routinely analyzed the electrophysiological traces to estimate the depth of insertion. For this, we calculated variance in the FFT of the voltage traces to identify the transition from low-variance exterior channels and high-variance intracortical channels. The estimated depth based on this approach matched well with the estimated depth based on images of the electrode at the site of penetration into the brain. Using this combination of approaches, the estimated probe depths were thus likely to be accurate within 50-100 μm. Additionally, in a subset of experiments, probe tracks were labeled by coating the probe with fluorescent dye, and visualized in subsequently prepared brain slices with epifluorescence optics to verify accurate placement of the probes in the M2 and/or RSC.

Model based analysis. We fit the following model to the locally evoked activity in RSC:

$$A_{RSC}(t-u) = ms(t) / \left| a_0 + \sum_{\Delta t}^{T} s(t-\Delta t) \right|$$

where *m* is a scaling factor, $J(x)$=0 for x<0 and $J(x)$=*x* for $x \geq 0$, a_0 regulates the strength of decay, Δt indexes the delays over which stimulation affects activity (Δt =0 would be instantaneous activation), *s(t)* is the optical stimulus and *u* is the delay. The three parameters of this model *u*, *m*, and a_0 are optimized to minimize the root mean squared error (RMSE) of the model using the MATLAB fminsearch function.

We fit the following model to the downstream activity in M2:

$$A_{M2}(t) = \vartheta \left(m \sum_{\Delta t=1}^{T} e^{\frac{-\Delta t}{\tau_{interact}}} A_{RSC}(t-\Delta t) - \theta \right) + c$$

where *m* is a scaling factor, $J(x)$=0 for x<0 and $J(x)$=*x* for $x \geq 0$, Δt indexes the past input from RSC, $t_{interact}$ is the interaction time constant, $A_{RSC}(t)$ is the activity in area RSC, q is the threshold, and *c* is the baseline. The four parameters of this model *c*, q, $t_{interact}$, and *m* are also optimized to minimize the RMSE.

Statistical analyses. Group data were compared using appropriate non-parametric tests (e.g. rank sum tests for unpaired and sign tests for paired data) as indicated, with significance defined as $p < 0.05$. Plots with error bars represent the sample medians ± median absolute deviations (m.a.d.) (calculated with the Matlab function, mad.m).

ACKNOWLEDGEMENTS: We thank C. Maguire for technical assistance. We thank David Heeger and Mike Landy for useful discussions. Grant support: NIH (NINDS grant NS061963; NIBIB grant EB017695).

FIGURES

Figure 1. Viral labeling and instrumentation to study inter-areal signaling in the corticocortical projection from retrosplenial (RSC) to posterior secondary motor (M2) cortex.

(A) Virus injection in RSC infects somata at the injection site, resulting in anterograde labeling of RSC axons projecting to M2. Right: epifluorescence image of the dorsal surface of the brain of an anesthetized mouse, showing labeled axons projecting from RSC to posterior M2.

(B) Coronal brain slices showing labeled axons in M2, and the track of a dye-coated linear array. Left: bright-field image. M2 is between the primary motor (M1) and anterior cingulate (AC) cortices. Right: epifluorescence image, showing labeled axons from RSC within M2, and the track of a dye-coated linear array (probe) that had been inserted in M2.

(C) Depiction of experimental set-up showing aspects of the hardware control apparatus and wiring. An optical fiber (blue) was placed over, and a silicon probe was inserted into, each of the two cortical areas. The optical fibers were coupled to blue light-emitting diodes (LEDs). See Methods for additional details.

Figure 2. RSC photostimulation drives downstream M2 activity.

(A) Experimental paradigm: RSC neurons were infected with AAV to express ChR2, and photostimuli were applied to RSC while recording multi-unit activity in M2, to sample orthodromically generated activity in the downstream area.

(B) Example traces across channels for a single trial of photostimulation (10-ms duration, 100% intensity; marked by blue band).

(C) Example traces from one recording channel (black trace in panel D) over multiple trials. Photostimulation reliably generated post-stimulus spiking activity.

(D) Peristimulus time histogram showing the mean photo-evoked response across all channels and trials. Top: Example from an animal injected with AAV9-ChR2. Bottom: Example from an animal injected with AAV1-ChR2.

(E) Top: Injection of muscimol into the M2 cortex abolished most of the evoked activity. Bottom: Little activity was detected when the probe was placed in a laterally adjacent cortical area (primary motor cortex, M1).

Figure 3. Comparison of local RSC and downstream M2 activity evoked by RSC photostimulation.

(A) Experimental paradigm: RSC neurons were infected with AAV to express ChR2, and photostimuli were applied to RSC while recording multi-unit activity in both M2 (orthodromically driven) and RSC (locally driven).

(B) Activity recorded on the RSC probe during RSC stimulation in animals injected with AAV9-ChR2. Red trace is the median response across 6 animals (traces for each animal shown in gray).

(C) Activity recorded on the M2 probe during the same experiment. Blue trace is the median response across animals.

(D) Overall activity on the RSC and M2 probes plotted together (peak-normalized).

(E) Amplitudes of responses (summed events) recorded on the RSC and M2 probes, plotted for each experiment (gray) and as the median across animals (blue). P-value calculated by 2-sided, paired sign test.

(F) Latencies (to peak) for responses recorded on the RSC and M2 probes. P-value calculated by 2-sided, paired sign test.

(G-K) Same, but for experiments using AAV1-ChR2.

Figure 4. Parametric characterization of orthodromic (forward) driving.

(A) Light pulses with a total of 25 different combinations of stimulus intensities (20, 40, 60, 80, and 100% relative to maximum) and durations (1, 5, 10, 20, and 50 ms) were used to photostimulate the RSC.

(B) Activity recorded locally in RSC (red) in response to RSC photostimulation using the stimuli shown in panel A. Each trace is the median response across AAV9-ChR2 animals (n = 6 experiments).

(C) Activity recorded simultaneously in M2 (green) in the same experiments.

Figure 4—figure supplement 1. Parametric characterization of orthodromic (forward) driving: AAV1 data.

(A) Light pulses with a total of 25 different combinations of stimulus intensities (20, 40, 60, 80, and 100% relative to maximum) and durations (1, 5, 10, 20, and 50 ms) were used to photostimulate the RSC.

(B) Activity recorded locally in RSC (red) in response to RSC photostimulation using the stimuli shown in panel A. Each trace is the median response across AAV1-ChR2 animals (*n* = 6 experiments).

(C) Activity recorded simultaneously in M2 (green) in the same experiments.

Figure 5. A simple two-stage model captures the major features of orthodromic driving.

(A) Depiction of the modeling. The first stage is the conversion of light pulses into local activity in the RSC, which is modeled by convolving the step pulses of light with a step function scaled by a decay process. The second stage is the conversion of the upstream RSC activity into downstream M2 activity, which is modeled by convolving the RSC activity with an exponential process with a temporal lag. The models were fitted to the data over the 0-60 ms poststimulus interval. See text for additional details.

(B) The fitted RSC responses (red) were generated by modeling the light pulse→RSC transfer function as described in panel A. The AAV9 data traces (gray) are shown superimposed.

(C) Plot of the residuals (black trace), calculated by subtracting the mean fitted traces (red) from the mean data traces (gray).

(D) The fitted M2 responses (green) were generated by modeling the RSC→M2 transfer function as described in panel A. The data traces (gray) are shown superimposed.

(E) Plot of the residuals (black trace), calculated by subtracting the mean fitted traces (green) from the mean data traces (gray).

Figure 5—figure supplement 1. A simple two-stage model captures the major features of orthodromic driving: AAV1 data.

(A) The fitted RSC responses (red) were generated by modeling the light pulse→RSC transfer function as described in panel A. The data traces are shown superimposed in gray.

(B) Plot of the residuals (black trace), calculated by subtracting the mean fitted traces (red) from the mean data traces (gray).

(C) The fitted M2 responses (green) were generated by modeling the RSC→M2 transfer function as described in panel A. The data traces are shown superimposed in gray.

(D) Plot of the residuals (black trace), calculated by subtracting the mean fitted traces (green) from the mean data traces (gray).

Figure 6. Analysis of orthodromically driven response amplitudes and latencies.

(A) Amplitudes (calculated as the summed events) of the responses recorded on the RSC and M2 probes during RSC photostimulation, for each of the 25 combinations of stimulus intensity and duration (gray) along with the median values (blue). Experiments with AAV9 are shown on the left, and those with AAV1 in the middle. P-values calculated by 2-sided, paired sign test.

(B) Driving ratios (defined as the ratio of activity generated locally in RSC over that generated remotely in M2) calculated for AAV9 and AAV1 experiments, plotted as the median (across the 25 stimulus parameter combinations) ± m.a.d.

(C) Same, but for latencies. Scaling of the vertical axes is set to facilitate comparison to similar plots in Fig. 8.

Figure 6—figure supplement 1. Dependence of RSC responses on stimulus intensity and duration.

(A) Top: For the RSC recordings, response amplitudes are plotted as a function of stimulus intensity; each line is for data recorded at constant stimulus duration, as indicated. Bottom: Same analysis, for the modeled responses.

(B) Top: Same curves as in panel A, but peak-normalized. Response amplitudes grew approximately linearly with stimulus intensity. Bottom: Same analysis, for the modeled responses.

(C) Top: Same as panel A, but showing responses as a function of stimulus duration. Bottom: Same analysis, for the modeled responses.

(D) Top: Same curves as in panel D, but peak-normalized. Bottom: Same analysis, for the modeled responses.

Response amplitudes grew sub-linearly (approximately logarithmically) with stimulus duration. Bottom: Same analysis, for the modeled responses.

Figure 6—figure supplement 2. Dependence of M2 responses on stimulus intensity and duration.

(A) Top: For the M2 recordings, response amplitudes are plotted as a function of stimulus intensity; each line is for data recorded at constant stimulus duration, as indicated. Bottom: Same analysis, for the modeled responses.

(B) Top: Same curves as in panel A, but peak-normalized. Response amplitudes grew approximately linearly with stimulus intensity. Bottom: Same analysis, for the modeled responses.

(C) Top: Same as panel A, but showing responses as a function of stimulus duration. Bottom: Same analysis, for the modeled responses.

(D) Top: Same curves as in panel D, but peak-normalized. Bottom: Same analysis, for the modeled responses. Response amplitudes grew sub-linearly (approximately logarithmically) with stimulus duration. Bottom: Same analysis, for the modeled responses.

Figure 7. Driving in reverse: antidromic propagation.

(A) Experimental paradigm: RSC neurons were infected with AAV to express ChR2, and photostimuli were applied to M2 (to stimulate axons of RSC neurons) while recording multi-unit activity in both M2 (locally driven) and RSC (antidromically driven).

(B) Activity recorded on the RSC probe during RSC stimulation in an animal injected with AAV9-ChR2. Red trace is the median response across animals (traces for each animal shown in gray).

(C) Activity recorded on the M2 probe during the same experiment. Blue trace is the median response across animals.

(D) Overall activity on the RSC and M2 probes plotted together (peak-normalized).

(E) Amplitudes of responses (summed events) recorded on the RSC and M2 probes, plotted for each experiment (gray) and as the median across animals (blue). P-value calculated by 2-sided, paired sign test.

(F) Latencies (to peak) for responses recorded on the RSC and M2 probes.

(G-K) Same, but for experiments using AAV1-ChR2.

(L) Response amplitudes across all 25 stimulus parameter combinations (gray), with the overall median (blue), for AAV9 (left) and AAV1 (middle) experiments. Right: Driving ratios (defined as the ratio of activity generated locally in RSC over that generated remotely in M2) calculated for AAV9 and AAV1 experiments, plotted as the median (across the 25 stimulus parameter

678 combinations) ± m.a.d. Scaling of the vertical axes is set to facilitate comparison to similar plots
679 in Fig. 6.
680 (M) Same, for latencies.
681
682 **Figure 8. Laminar analysis.**
683 (A) Left: Image of 32-channel silicon probe, taken through the ocular of a stereoscope, showing
684 5 visible contacts above the penetration site into the cortex. Distance between contacts is 50 µm.
685 Right: Plot of the variance in the FFT of the traces collected on the first 20 channels of the probe,
686 showing an abrupt increase for channels deeper than the 6th contact (dashed line).
687 (B) Average peristimulus-time histogram across all channels in a 32-channel array in M2 during
688 RSC photostimulation, plotted on a color scale.
689 (C) Laminar profiles recorded for each animal (left) and overall profile (mean ± s.e.m., n = 9
690 mice injected with AAV1-ChR2) as calculated for the response interval (red) and baseline (blue).
691 (D) In *ex vivo* brain slice experiments, cell-attached recordings were made from layer 2/3 and
692 layer 5B neurons while photostimulating RSC axons. Left: Example traces showing spiking
693 response in the layer 5B neuron. Right: The mean number of evoked spikes was calculated for
694 each neuron, and plotted as a cumulative histogram of spike probability. Layer 5B neurons
695 spiked significantly more than layer 2/3 neurons (p = 0.009, rank-sum test; median spikes were 0
696 vs 1 for layer 2/3 vs 5B, respectively; n = 15 layer 2/3 and 15 layer 5B neurons).
697
698

699 **REFERENCES**

700

701 Arbib MA (2002) The Handbook of Brain Theory and Neural Networks, 2 Edition. Cambridge,
702 Massachusetts: MIT Press.
703 Bassett DS, Sporns O (2017) Network neuroscience. Nat Neurosci 20:353-364.
704 doi:10.1038/nn.4502
705 Bernander O, Koch C, Douglas RJ (1994) Amplification and linearization of distal synaptic input
706 to cortical pyramidal cells. J Neurophysiol 72:2743-2753.
707 Brown CE, Aminoltejari K, Erb H, Winship IR, Murphy TH (2009) In vivo voltage-sensitive dye
708 imaging in adult mice reveals that somatosensory maps lost to stroke are replaced over
709 weeks by new structural and functional circuits with prolonged modes of activation
710 within both the peri-infarct zone and distant sites. J Neurosci 29:1719-1734.
711 doi:10.1523/JNEUROSCI.4249-08.2009
712 Carandini M (2012) From circuits to behavior: a bridge too far? Nat Neurosci 15:507-509.
713 doi:10.1038/nn.3043
714 Carandini M, Heeger DJ, Movshon JA (1997) Linearity and normalization in simple cells of the
715 macaque primary visual cortex. J Neurosci 17:8621-8644.
716 Chapman B, Zahs KR, Stryker MP (1991) Relation of cortical cell orientation selectivity to
717 alignment of receptive fields of the geniculocortical afferents that arborize within a single
718 orientation column in ferret visual cortex. J Neurosci 11:1347-1358.
719 Chatterjee S, Callaway EM (2003) Parallel colour-opponent pathways to primary visual cortex.
720 Nature 426:668-671. doi:10.1038/nature02167
721 Ermentrout GB, Terman DH (2010) Mathematical Foundations of Neuroscience. New York:
722 Springer Verlag.
723 Felleman DJ, Van Essen DC (1991) Distributed hierarchical processing in the primate cerebral
724 cortex. Cereb Cortex 1:1-47.
725 Glasser MF, Coalson TS, Robinson EC, Hacker CD, Harwell J, Yacoub E, Ugurbil K, Andersson
726 J, Beckmann CF, Jenkinson M, Smith SM, Van Essen DC (2016) A multi-modal
727 parcellation of human cerebral cortex. Nature 536:171-178. doi:10.1038/nature18933
728 Grosenick L, Marshel JH, Deisseroth K (2015) Closed-loop and activity-guided optogenetic
729 control. Neuron 86:106-139. doi:10.1016/j.neuron.2015.03.034
730 Harris KD, Shepherd GM (2015) The neocortical circuit: themes and variations. Nat Neurosci
731 18:170-181. doi:10.1038/nn.3917
732 Histed MH, Bonin V, Reid RC (2009) Direct activation of sparse, distributed populations of
733 cortical neurons by electrical microstimulation. Neuron 63:508-522.
734 doi:10.1016/j.neuron.2009.07.016
735 Hooks BM, Mao T, Gutnisky D, Yamawaki N, Svoboda K, Shepherd GMG (2013) Organization
736 of cortical and thalamic input to pyramidal neurons in mouse motor cortex. J Neurosci
737 33:748-760. doi:10.1523/JNEUROSCI.4338-12.2013
738 Jbabdi S, Sotiropoulos SN, Haber SN, Van Essen DC, Behrens TE (2015) Measuring
739 macroscopic brain connections in vivo. Nat Neurosci 18:1546-1555. doi:10.1038/nn.4134
740 Kinnischtzke AK, Simons DJ, Fanselow EE (2014) Motor cortex broadly engages excitatory and
741 inhibitory neurons in somatosensory barrel cortex. Cereb Cortex 24:2237-2248.
742 doi:10.1093/cercor/bht085

743 Kinnischtzke AK, Fanselow EE, Simons DJ (2016) Target-specific M1 inputs to infragranular S1
744 pyramidal neurons. J Neurophysiol 116:1261-1274. doi:10.1152/jn.01032.2015
745 La Camera G, Rauch A, Thurbon D, Luscher HR, Senn W, Fusi S (2006) Multiple time scales of
746 temporal response in pyramidal and fast spiking cortical neurons. J Neurophysiol
747 96:3448-3464. doi:10.1152/jn.00453.2006
748 Lim DH, Mohajerani MH, Ledue J, Boyd J, Chen S, Murphy TH (2012) In vivo large-scale
749 cortical mapping using channelrhodopsin-2 stimulation in transgenic mice reveals
750 asymmetric and reciprocal relationships between cortical areas. Front Neural Circuits
751 6:11. doi:10.3389/fncir.2012.00011
752 Lin JY, Lin MZ, Steinbach P, Tsien RY (2009) Characterization of engineered channelrhodopsin
753 variants with improved properties and kinetics. Biophys J 96:1803-1814.
754 doi:10.1016/j.bpj.2008.11.034
755 Maguire EA (2001) The retrosplenial contribution to human navigation: a review of lesion and
756 neuroimaging findings. Scandinavian journal of psychology 42:225-238.
757 Manita S, Suzuki T, Homma C, Matsumoto T, Odagawa M, Yamada K, Ota K, Matsubara C,
758 Inutsuka A, Sato M, Ohkura M, Yamanaka A, Yanagawa Y, Nakai J, Hayashi Y, Larkum
759 ME, Murayama M (2015) A Top-Down Cortical Circuit for Accurate Sensory
760 Perception. Neuron 86:1304-1316. doi:10.1016/j.neuron.2015.05.006
761 Mao T, Kusefoglu D, Hooks BM, Huber D, Petreanu L, Svoboda K (2011) Long-range neuronal
762 circuits underlying the interaction between sensory and motor cortex. Neuron 72:111-
763 123. doi:10.1016/j.neuron.2011.07.029
764 Miesenbock G (2009) The optogenetic catechism. Science 326:395-399.
765 doi:10.1126/science.1174520
766 Miller KD (2016) Canonical computations of cerebral cortex. Curr Opin Neurobiol 37:75-84.
767 doi:10.1016/j.conb.2016.01.008
768 Minoshima S, Giordani B, Berent S, Frey KA, Foster NL, Kuhl DE (1997) Metabolic reduction
769 in the posterior cingulate cortex in very early Alzheimer's disease. Ann Neurol 42:85-94.
770 doi:10.1002/ana.410420114
771 Misic B, Sporns O (2016) From regions to connections and networks: new bridges between brain
772 and behavior. Curr Opin Neurobiol 40:1-7. doi:10.1016/j.conb.2016.05.003
773 Nagel G, Brauner M, Liewald JF, Adeishvili N, Bamberg E, Gottschalk A (2005) Light
774 activation of channelrhodopsin-2 in excitable cells of *Caenorhabditis elegans* triggers
775 rapid behavioral responses. Curr Biol 15:2279-2284. doi:10.1016/j.cub.2005.11.032
776 Nagel G, Szellas T, Huhn W, Kateriya S, Adeishvili N, Berthold P, Ollig D, Hegemann P,
777 Bamberg E (2003) Channelrhodopsin-2, a directly light-gated cation-selective membrane
778 channel. Proc Natl Acad Sci U S A 100:13940-13945. doi:10.1073/pnas.1936192100
779 Nowak LG, Bullier J (1998) Axons, but not cell bodies, are activated by electrical stimulation in
780 cortical gray matter. II. Evidence from selective inactivation of cell bodies and axon
781 initial segments. Exp Brain Res 118:489-500.
782 Oh SW et al. (2014) A mesoscale connectome of the mouse brain. Nature 508:207-214.
783 doi:10.1038/nature13186
784 Petreanu L, Huber D, Sobczyk A, Svoboda K (2007) Channelrhodopsin-2-assisted circuit
785 mapping of long-range callosal projections. Nat Neurosci 10:663-668.
786 doi:10.1038/nn1891
787 Petreanu L, Mao T, Sternson SM, Svoboda K (2009) The subcellular organization of neocortical
788 excitatory connections. Nature 457:1142-1145. doi:10.1038/nature07709

789 Petrof I, Viaene AN, Sherman SM (2015) Properties of the primary somatosensory cortex
790 projection to the primary motor cortex in the mouse. J Neurophysiol 113:2400-2407.
791 doi:10.1152/jn.00949.2014
792 Raastad M, Shepherd GM (2003) Single-axon action potentials in the rat hippocampal cortex. J
793 Physiol 548:745-752. doi:10.1113/jphysiol.2002.032706
794 Rolls ET (2016) Cerebral Cortex: Principles of Operation. Oxford: Oxford University Press.
795 Sabatini BL, Regehr WG (1999) Timing of synaptic transmission. Annu Rev Physiol 61:521-
796 542. doi:10.1146/annurev.physiol.61.1.521
797 Sato TK, Hausser M, Carandini M (2014) Distal connectivity causes summation and division
798 across mouse visual cortex. Nat Neurosci 17:30-32. doi:10.1038/nn.3585
799 Sherman SM, Guillery RW (2011) Distinct functions for direct and transthalamic corticocortical
800 connections. J Neurophysiol 106:1068-1077. doi:10.1152/jn.00429.2011
801 Sreenivasan V, Esmaeili V, Kiritani T, Galan K, Crochet S, Petersen CC (2016) Movement
802 Initiation Signals in Mouse Whisker Motor Cortex. Neuron 92:1368-1382.
803 doi:10.1016/j.neuron.2016.12.001
804 Sugar J, Witter MP, van Strien NM, Cappaert NL (2011) The retrosplenial cortex: intrinsic
805 connectivity and connections with the (para)hippocampal region in the rat. An interactive
806 connectome. Front Neuroinform 5:7. doi:10.3389/fninf.2011.00007
807 Suter BA, Shepherd GMG (2015) Reciprocal interareal connections to corticospinal neurons in
808 mouse m1 and s2. J Neurosci 35:2959-2974. doi:10.1523/JNEUROSCI.4287-14.2015
809 Suter BA, Migliore M, Shepherd GMG (2013) Intrinsic electrophysiology of mouse
810 corticospinal neurons: a class-specific triad of spike-related properties. Cerebral Cortex
811 23:1965-1977. doi:10.1093/cercor/bhs184
812 Vann SD, Aggleton JP, Maguire EA (2009) What does the retrosplenial cortex do? Nat Rev
813 Neurosci 10:792-802. doi:10.1038/nrn2733
814 Wark B, Lundstrom BN, Fairhall A (2007) Sensory adaptation. Curr Opin Neurobiol 17:423-
815 429. doi:10.1016/j.conb.2007.07.001
816 Yamawaki N, Shepherd GMG (2015) Synaptic circuit organization of motor corticothalamic
817 neurons. J Neurosci 35:2293-2307. doi:10.1523/JNEUROSCI.4023-14.2015
818 Yamawaki N, Radulovic J, Shepherd GM (2016) A corticocortical circuit directly links
819 retrosplenial cortex to M2 in the mouse. J Neurosci 36:9365-9374.
820 doi:10.1523/JNEUROSCI.1099-16.2016
821 Yang W, Carrasquillo Y, Hooks BM, Nerbonne JM, Burkhalter A (2013) Distinct balance of
822 excitation and inhibition in an interareal feedforward and feedback circuit of mouse
823 visual cortex. J Neurosci 33:17373-17384. doi:10.1523/JNEUROSCI.2515-13.2013
824 Zingg B, Hintiryan H, Gou L, Song MY, Bay M, Bienkowski MS, Foster NN, Yamashita S,
825 Bowman I, Toga AW, Dong HW (2014) Neural networks of the mouse neocortex. Cell
826 156:1096-1111. doi:10.1016/j.cell.2014.02.023
827
828

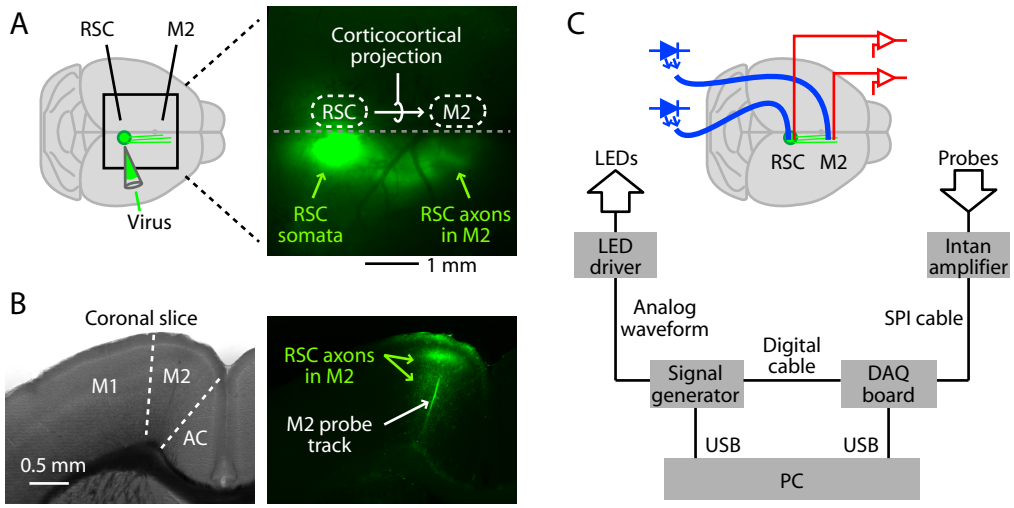

Figure 1

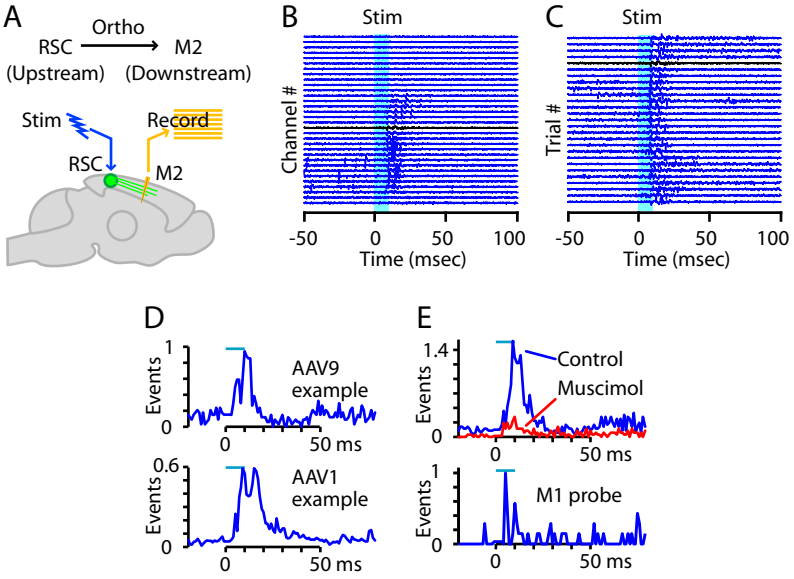

Figure 2

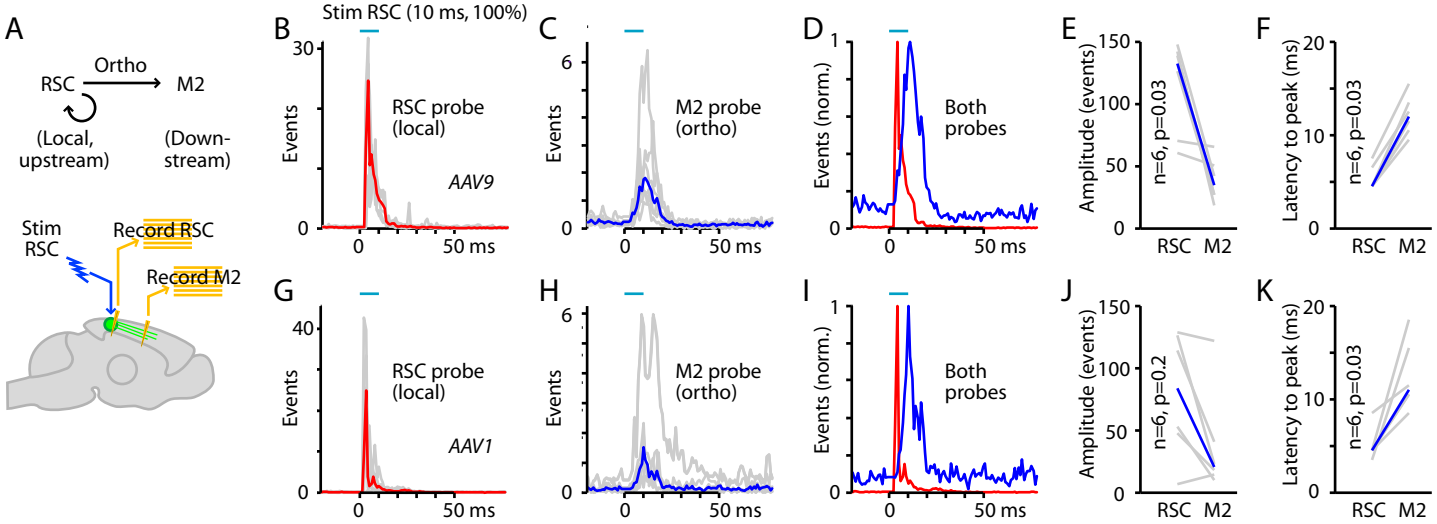

Figure 3

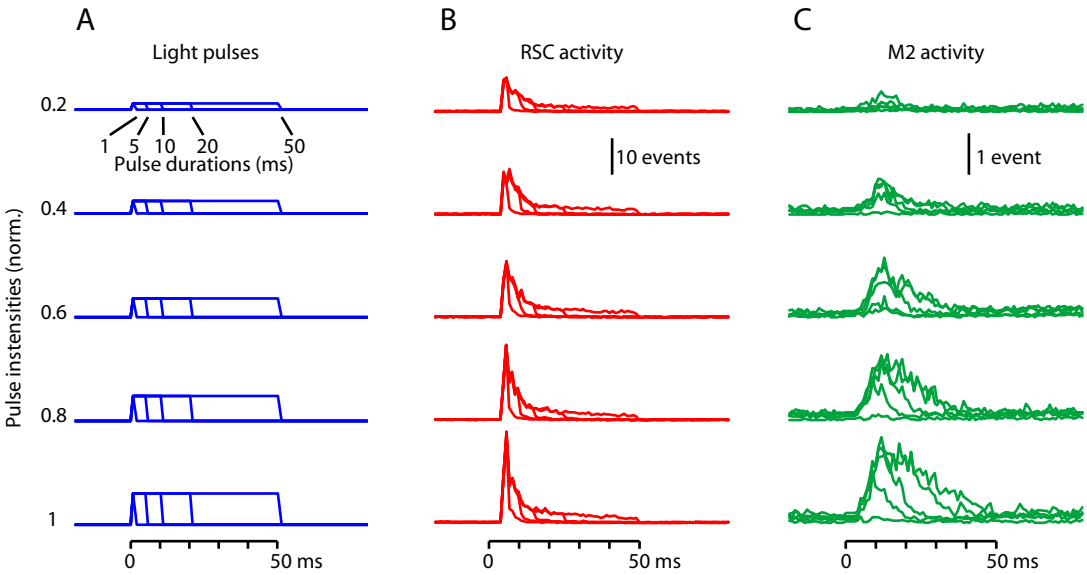

Figure 4

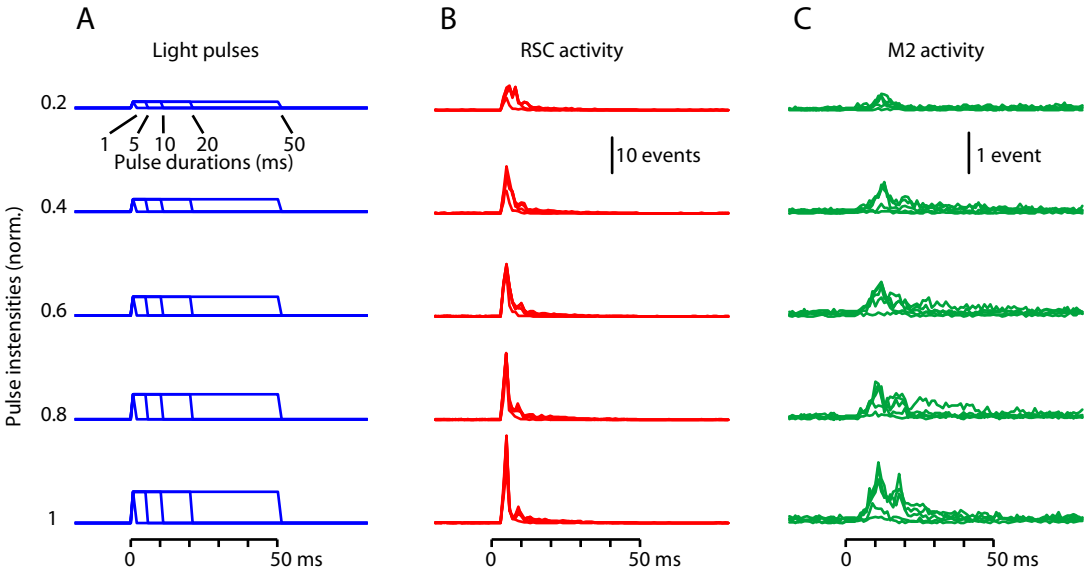

Figure 4--figure supplement 1

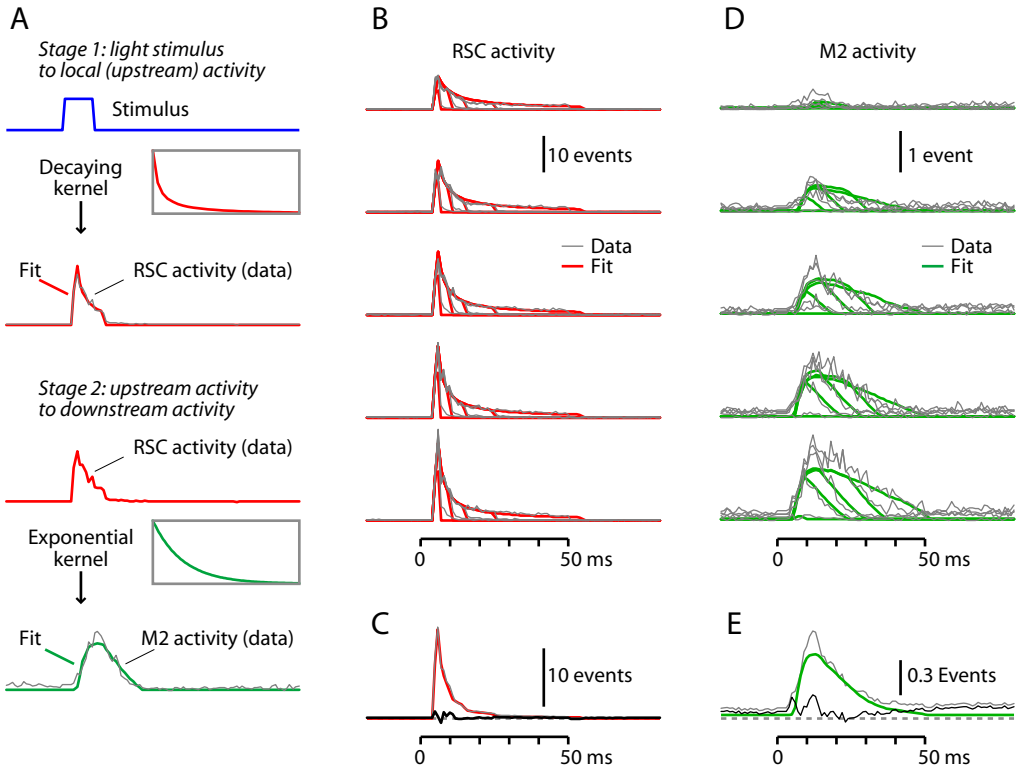

Figure 5

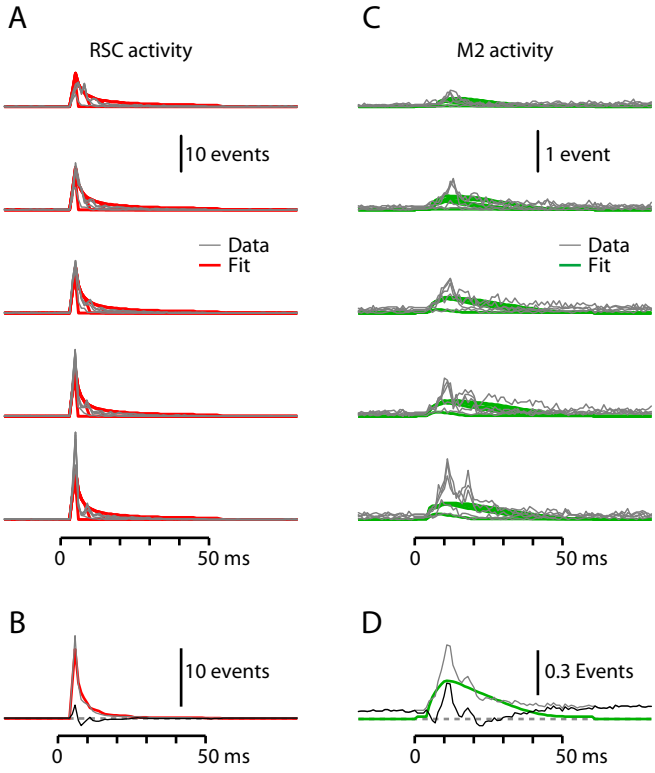

Figure 5--figure supplement 1

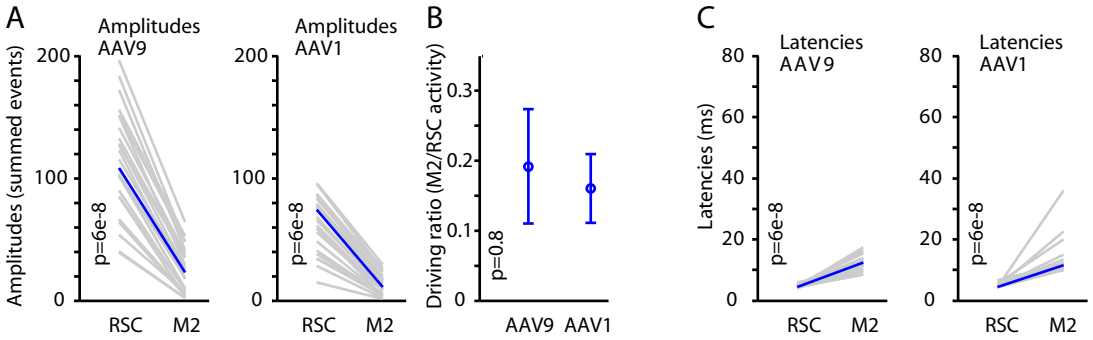

Figure 6

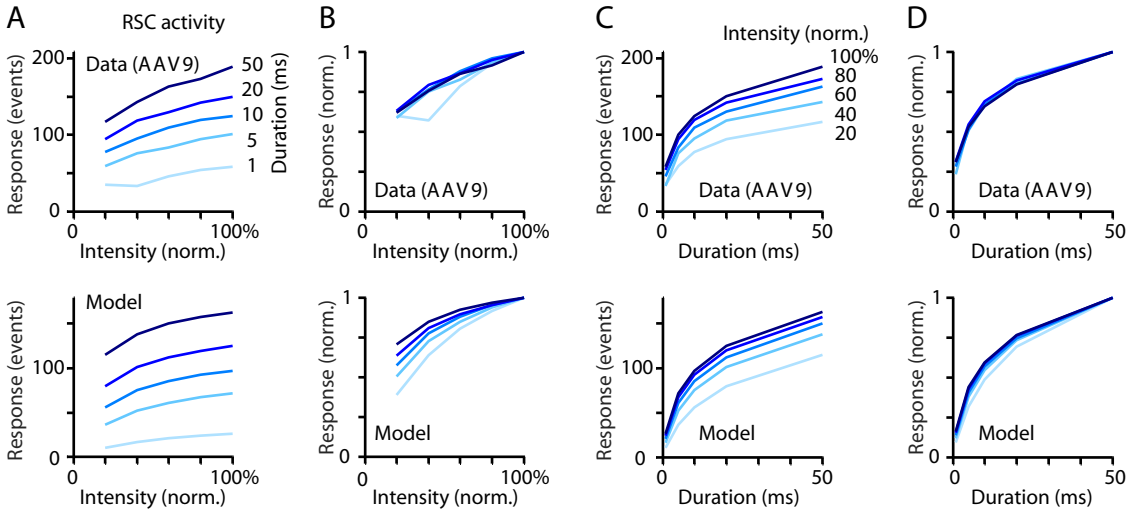

Figure 6---figure supplement 1

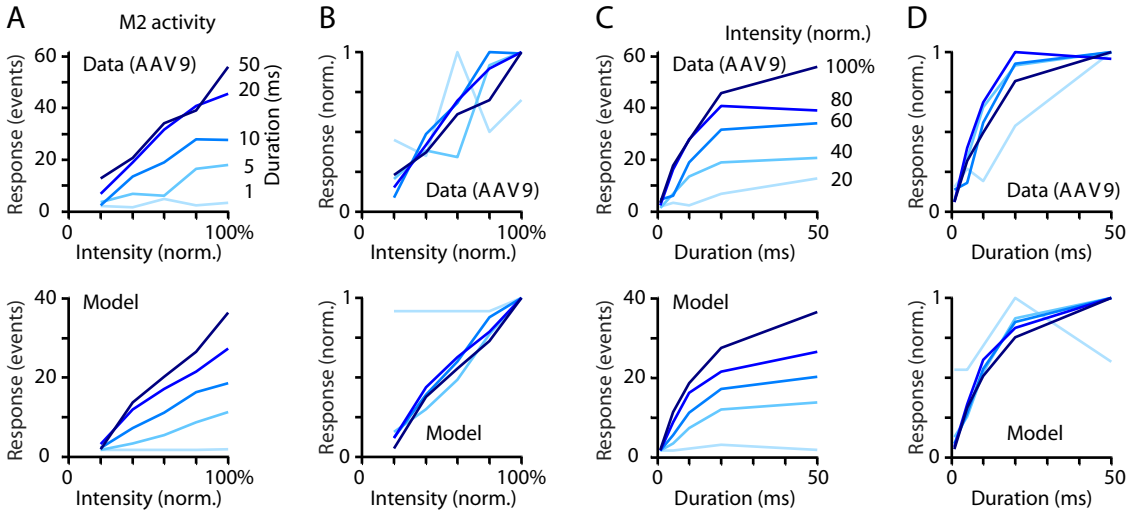

Figure 6---figure supplement 2

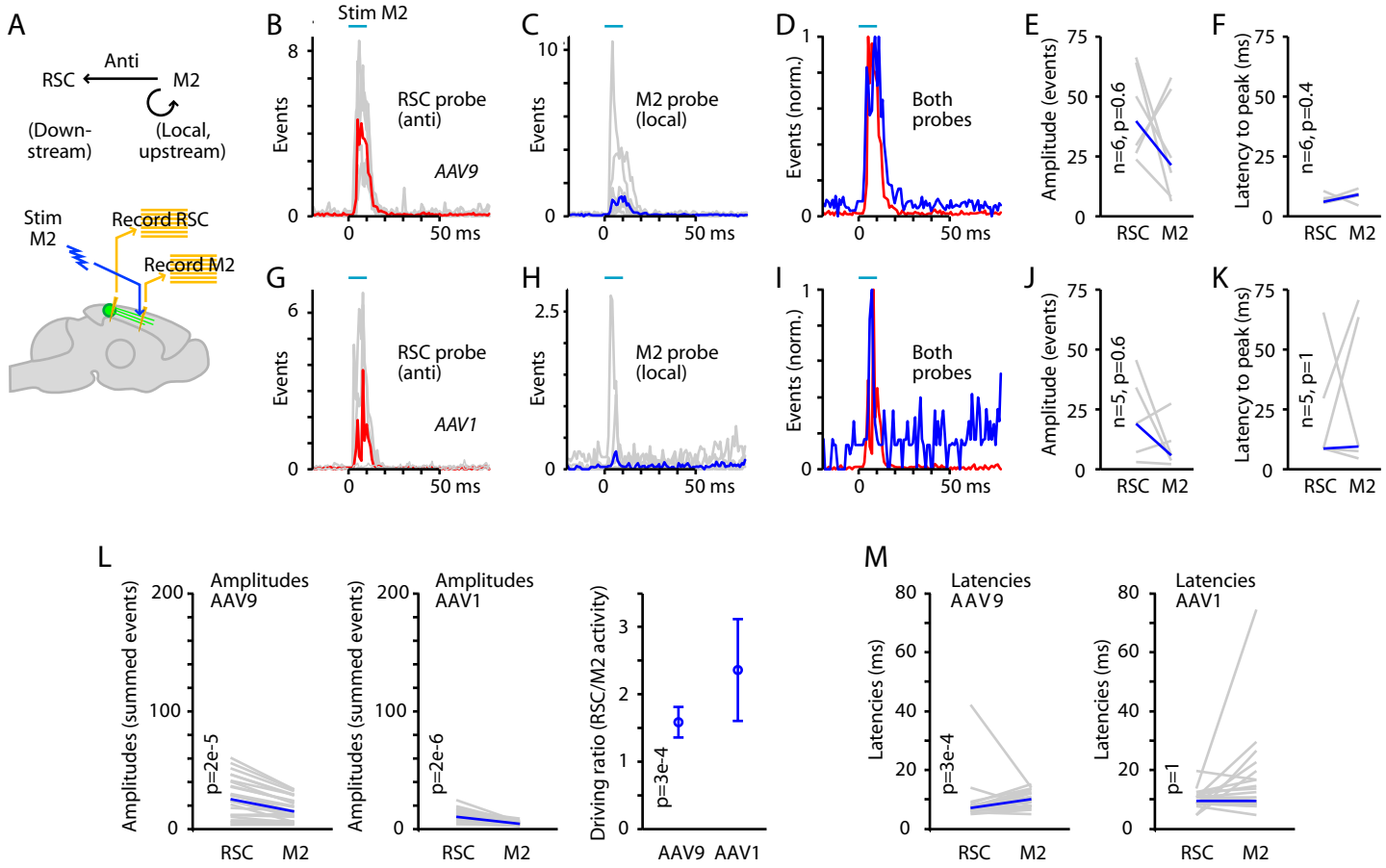

Figure 7

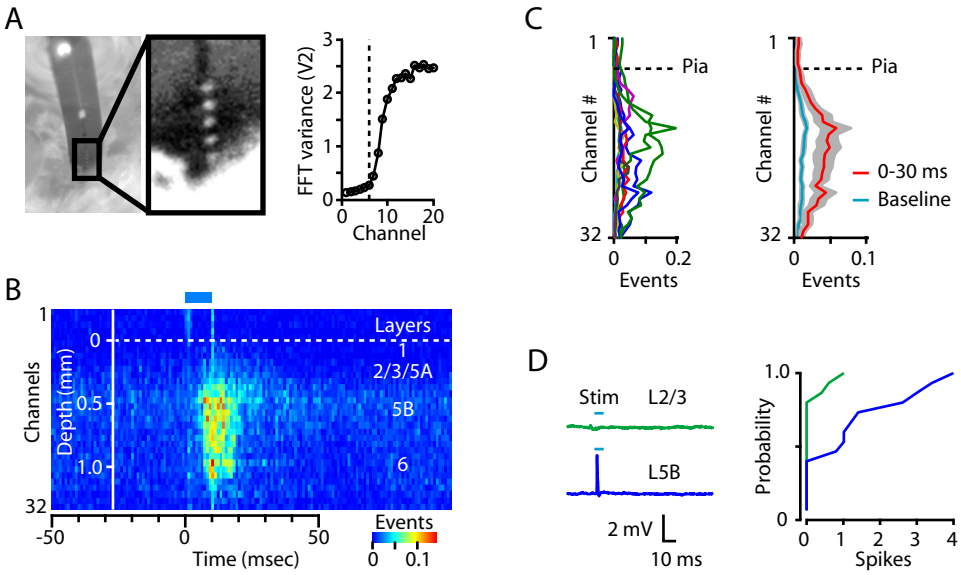

Figure 8